# Recombination Rate Analysis of InGaN-Based Red-Emitting Light-Emitting Diodes

Haotian Xue<sup>®</sup>, Syed Ahmed Al Muyeed<sup>®</sup>, Elia Palmese<sup>®</sup>, Daniel Rogers<sup>®</sup>, Renbo Song, Nelson Tansu, *Fellow, IEEE*, and Jonathan J. Wierer, Jr.<sup>®</sup>, *Senior Member, IEEE* 

Abstract—The recombination rates are measured and analyzed for red-emitting InGaN light-emitting diodes (LEDs) to better understand the factors that limit their efficiency. InGaN/AlGaN/GaN multiple quantum well (MQWs) are grown with x≥0.28 in the In<sub>x</sub>Ga<sub>1-x</sub>N quantum well. The Al<sub>y</sub>Ga<sub>1-v</sub>N interlayers (ILs) with high Al-content (y>0.8) are employed because they result in smoother surfaces with smaller V-pits and higher photoluminescence efficiency. The IL-MQWs are formed on GaN and InzGa1-zN/GaN superlattice (SL) underlayers (ULs) with z = 0.015, 0.025, and 0.065. Differences in B coefficients (radiative recombination) within this set result from changes in wavefunction overlap caused by differences in layer thickness and composition in the IL-MQW. IL-MQWs grown on SL-ULs have A coefficients (Shockley-Reed-Hall recombination) that are lower than expected, indicating that the SL-ULs help reduce defect formation. Compared to shorter wavelength InGaN-based LEDs, the B coefficients are  $\sim 100$  times lower due to lower wavefunction overlap. A and C coefficients are higher because of a higher number of defects.

Index Terms—Light-emitting diodes (LEDs), InGaN multiple quantum well, recombination rates, interlayers, differential carrier lifetime, red LED, ABC coefficients, metal-organic chemical vapor deposition (MOCVD).

### I. Introduction

II-NITRIDE light-emitting diodes (LEDs) most notable application has been in solid-state lighting [1], [2]. Recently, research has focused on using them for efficient and large color gamut emissive displays, especially for augmented and virtual reality applications [3], [4]. In emissive displays, the LEDs are individual pixels, requiring smaller-sized micro-LEDs that emit efficiently at blue, green, and red wavelengths. InGaN-based LEDs are becoming the emitter of choice for

Manuscript received 28 October 2022; revised 26 January 2023; accepted 14 February 2023. Date of publication 22 February 2023; date of current version 28 February 2023. This work was supported by the U.S. National Science Foundation Award 2204317. (Corresponding author: Haotian Xue.)

Haotian Xue, Elia Palmese, Daniel Rogers, and Jonathan J. Wierer, Jr. are with the Department of Electrical and Computer Engineering, North Carolina State University, Raleigh, NC 27695 USA (e-mail: hxue8@ncsu.edu; jjwierer@ncsu.edu).

Syed Ahmed Al Muyeed is with Google, Inc., Fremont, CA 94539 USA (e-mail: muyeed@alum.lehigh.edu).

Renbo Song is with the Department of Electrical and Computer Engineering, Lehigh University, Bethlehem, PA 18015 USA.

Nelson Tansu is with the School of Electrical and Mechanical Engineering (EME), Institute for Photonics and Advanced Sensing (IPAS), The University of Adelaide, Adelaide, SA 5005, Australia (e-mail: nelson.tansu@adelaide.edu.au).

Color versions of one or more figures in this article are available at https://doi.org/10.1109/JQE.2023.3246981.

Digital Object Identifier 10.1109/JQE.2023.3246981

next-generation emissive displays as they can cover the entire visible spectrum by tuning the In-content in the InGaN quantum wells (QWs) [5].

State-of-the-art violet and blue light-emitting LEDs and laser diodes use InGaN-based multiple quantum wells (MQWs) as the active region [5]. These MQWs emit at green to red wavelengths by increasing the In-content in the QWs (x≥0.20) [6]. However, realizing high efficiencies at longer wavelengths has proven difficult, and this problem is called the "green gap" [1], [5]. Several reasons are typically given for the green gap, including lattice mismatch and defect formation [7], [8], phase separation [9], [10], carrier localization due to fluctuations in InGaN composition [11], [12], [13], low growth temperatures [14], [15], and low electron-hole wavefunction overlap due to spontaneous and piezoelectric polarization [16], [17], [18].

It has been shown that using thin AlGaN interlayers (ILs) grown on top of InGaN OWs results in a drastic improvement in the external quantum efficiency at green-red wavelengths [19], [20], [21]. Using AlGaN ILs is not intuitive, and there are several possible reasons for the observed improvement. Scanning transmission electron microscope (STEM) images show that AlGaN ILs "cap" the InGaN QWs, producing smoother and more abrupt heterointerfaces than InGaN/GaN heterointerfaces [19], [22]. This suggests that the AlGaN IL reduces the out-diffusion of indium from the QWs, which is confirmed with higher indium concentration QWs with AlGaN ILs [22], [23]. Additionally, ILs enable higher temperature growth of the GaN barriers, and this higher temperature growth anneals the QW and the ILs. This annealing improves the material quality and reduces impurity incorporation [22]. This is contrary to standard InGaN/GaN MQWs, where higher growth temperatures of the barriers are avoided. All these effects increase the radiative recombination rate and, thus, the external quantum efficiency. Finally, introducing an AlGaN IL increases the piezoelectric polarization-induced electric field on the QW, which in principle, could lower overlap. However, this is offset by the higher energy barrier from the IL and the more abrupt heterointerface; the combination provides a slightly higher electron and hole wavefunction overlap [24]. This overlap improvement is shown in Figure 1(a). Standard InGaN/GaN QWs exhibit interface grading [25], and the AlGaN IL creates an abrupt heterointerface on top of the InGaN QW. The IL shifts the electron wavefunction into the QW, causing an increase in the overlap with the hole wavefunction.

0018-9197 © 2023 IEEE. Personal use is permitted, but republication/redistribution requires IEEE permission. See https://www.ieee.org/publications/rights/index.html for more information.

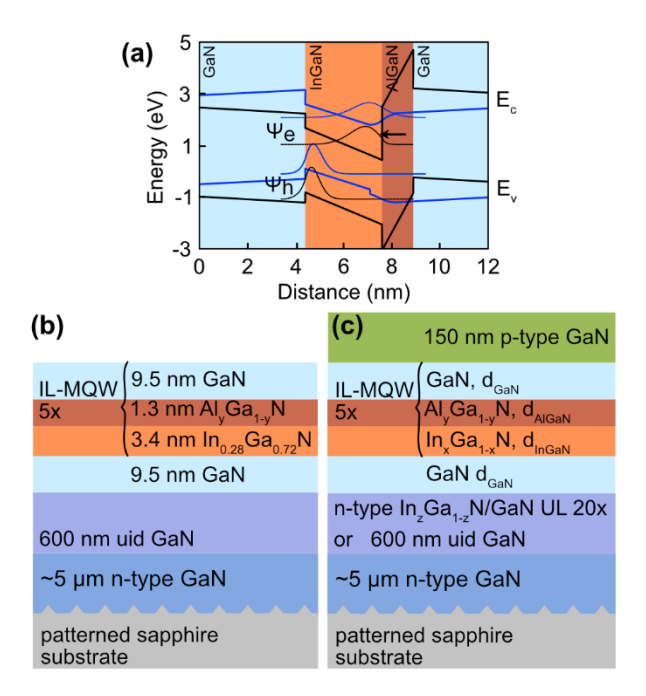


Fig. 1. Band diagram of a standard QW (blue lines) and IL-QW (black lines). The standard QW has a less abrupt heterointerface on the top, and the addition of the AlGaN interlayer shifts the electron wavefunction into the quantum well (arrow). Cross-sectional schematic of (b) InGaN/AlyGa $_{1-y}$ N/GaN IL-MQWs grown on GaN with different Al-content (y). Cross-sectional schematic of (c) InGaN/AlGaN/GaN IL-MQWs grown either a GaN layer or  $In_ZGa_{1-z}$ N/GaN superlattice underlayer (SL-UL) and capped with p-type GaN. The In-content (z) in the SL-UL is 0.015, 0.025, and 0.065.

Another well-known method to improve the light-emitting efficiency of InGaN QWs is to use an In-containing underlayer (UL) [15], [26], [27], [28]. A few reasons have been shown for how the UL improves the QWs. The first is that In atoms in the UL can stop surface defects from propagating into the active region, thus lowering defect recombination. The higher the In-content (without sacrificing surface quality) is, the more significant the improvement will be [29], [30]. Another reason is that carefully designed ULs can control the formation of V-pits in the QW active region. Reports have suggested that carrier localization effects due to V-pits can suppress non-radiative recombination [31]. Other reports have indicated that carrier injection through V-pits can improve the efficiency of long-wavelength emitters [32], [33]. Finally, the UL could provide partial strain relaxation for the InGaN QW, reducing its likelihood of forming defects [34], [35]. There has yet to be an investigation of the recombination rates in redemitting InGaN light emitters with IL-MQW active layers.

This article shows MOCVD growth and optical characterization of red-emitting LEDs with  $In_xGa_{1-x}N/Al_yGa_{1-y}N/GaN$  IL-MQWs grown on GaN and ULs. The ILs and ULs are used to achieve red-emission and allow for the measurement of recombination rates to better understand the factors that limit efficiency. First, IL-MQWs are grown with varying Al content in the  $Al_yGa_{1-y}N$  IL and grown on GaN without an UL. The IL with y=0.82 has the highest photoluminescence (PL) efficiency and shows a smoother surface morphology with regular, well-formed V-pits compared to other structures. Next, similar IL-MQWs are grown on a GaN layer and  $In_zGa_{1-z}N/GaN$ 

superlattice (SL) ULs at different growth temperatures to vary the In-content (z). Recombination rate measurements show that changes in the recombination rates can be explained by differences in wavefunction overlap in the quantum wells caused by layer thickness and concentration differences. There is a direct correlation between higher overlap with higher radiative recombination rates (or higher *B* coefficient). The growth of IL-MQWs on the SL-UL affects the Shockley-Reed-Hall (SRH) or defect recombination rates and suggests that the number of defects is lower when growing red-emitting QWs on SL-ULs. Finally, the red-emitting IL-MQWs are compared to shorter wavelength QWs. They have much lower *B* coefficients (~100 times lower) and higher *A* and *C* coefficients due to lower wavefunction overlap and a higher number of defects.

## II. EXPERIMENTAL METHODS

Two sets of structures with red-emitting IL-MQWs are grown in this study. The first set is to determine a suitable Al-content for the AlGaN IL. The second is a complete LED structure with IL-MQWs grown on different SL-ULs and placed within a p-n junction to measure recombination rates. All the structures are grown by metalorganic chemical vapor deposition (MOCVD) in a Veeco P-75 reactor. Several methods are used to characterize their properties. Layer thicknesses and compositions are determined by X-ray diffraction (XRD) by fitting omega-2theta curves along the (0002) reflection of GaN and by white light reflectance on either test samples or the final structures. Hall measurements are used to determine electron and hole concentrations. Atomic force microscopy (AFM) is used to measure surface morphology.

The first set of growths consists of five periods of InGaN/AlGaN/GaN IL-MQWs grown with different Al-content in the AlGaN IL. A schematic cross-section is shown in Fig. 1(b). The growth begins with a 600 nm thick unintentionally (uid) doped GaN layer on a commercially available n-type GaN template grown on c-plane patterned sapphire. This is followed by IL-MQWs grown at a pressure of 200 Torr. The InGaN QWs and AlGaN ILs are grown at a fixed temperature of 670 °C, as determined by in-situ pyrometry. The GaN barrier is grown next at an increased temperature of 880 °C. Then the temperature is reduced to grow the next InGaN QW, and this barrier-QW-IL sequence is repeated five times. All the growth parameters are kept constant in the IL-MQW except for the AlGaN IL. The Al content of the Al<sub>v</sub>Ga<sub>1-v</sub>N IL is varied by changing the gas phase ratio of the Al and Ga sources. The Al/(Al+Ga) molar gas phase ratios are 0.50, 0.70, and 0.90, and the resulting measured Al-contents are y = 0.43, 0.65, and 0.82. The lower measured values are likely caused by the non-ideal, low-temperature growth of AlGaN. The IL growth conditions are not necessarily ideal, and it has been shown that lowtemperature, high-Al content AlGaN growth results in rough surface morphology [21]. However, they are necessary to preserve the high In-content QW, and the subsequent hightemperature annealing before and during the barrier growth improves the smoothness and most likely the quality of the IL [22]. For the  $In_xGa_{1-x}N$  QWs, the In/(In+Ga) molar gas phase

TABLE I THICKNESSES, COMPOSITION, SPECTRAL FULL WIDTH AT HALF MAXI-MUM (FWHM), AND WAVEFUNCTION OVERLAP (I)

	$d_{InGaN}$		$d_{\mathrm{GaN}}$	$d_{AlGaN}$		FWHM	
Z	(nm)	X	(nm)	(nm)	у	(nm)	I
0	3.7	0.28	10.4	1.2	0.82	76	1.03×10 <sup>-1</sup>
0.015	3.3	0.27	9.5	1.2	0.82	64	1.72×10 <sup>-1</sup>
0.025	3.5	0.28	9.0	1.25	0.82	57	$1.44 \times 10^{-1}$
0.065	3.1	0.29	9.6	1.2	0.9	61	$2.14 \times 10^{-1}$

ratio is  $\sim 0.50$ , and the measured In composition is x = 0.28. The InGaN QWs, AlGaN ILs, and GaN barriers are  $\sim 3.4$  nm,  $\sim$  1.3 nm, and  $\sim$  9.3 nm thick, respectively.

The second set has IL-MQWs that are grown on GaN and different SL-ULs to measure recombination rates to assess their efficiencies. Four LED samples are grown, as shown in Fig 1(c). Three samples have SL-ULs with differing In-content, and a fourth with an uid-GaN layer. The SL-UL consists of 20 periods of n-type 1.8 nm thick InGaN and 2 nm thick GaN layers grown at 850 °C, 830 °C, and 780 °C, resulting in an In-content of z = 0.015, 0.025, and 0.065, respectively. They are grown at a V-III ratio of 51,000, and this high V-III ratio is chosen to produce smooth surfaces. The lower the growth temperature, the higher the In-content and V-pit size [7], [34], [36]. P-type GaN layers are grown on top of the IL-MQWs to form a p-n junction and to avoid modulation doping in the quantum wells [37]. The high In-content QWs need to be protected from high temperatures during the growth of the p-type layers. So, the p-type GaN is grown at 830 °C with TEGa due to its lower cracking temperature to achieve smoother surface morphology. (It is noted that the PL efficiency does not change with the addition of this p-GaN layer.) This 150 nm thick layer is grown with a high V-III ratio of 28,000 with a growth rate of 2.2 nm/min. The hole concentration and mobility are 10<sup>17</sup> cm<sup>-3</sup> and 6 cm<sup>2</sup>V<sup>-1</sup>s<sup>-1</sup>, respectively. Although not as conductive as p-type GaN grown with TMGa, it has smoother surface morphology at low temperatures. There are subtle differences in the thickness and alloy content of the IL-MQW layers listed in Table I. These are all due to run-to-run growth variations in the MOCVD reactor for this set and are determined by fitting the XRD data. The InGaN QW thicknesses and In-content vary from 3.1 nm to 3.7 nm and 0.28 to 0.296, respectively. The GaN barrier thickness varies from 9 nm to 10.4 nm. The AlGaN IL thickness and Al-content range from 1.2 nm to 1.25 nm and 0.82 to 0.9, respectively. These variations will result in differences in the wavefunction overlap of carriers in the QWs. To determine the wavefunction overlap, Schrodinger-Poisson modeling is performed. All structures are assumed to be pseudomorphic to GaN.

The wavefunction overlap  $(I = \int \psi_e^* \psi_h dx)$  is shown in the last column of Table I. The I is calculated using the nextnano<sup>3</sup> Schrödinger-Poisson solver [38] with the standard variables and a conduction band to bandgap offset of  $\Delta E_c \sim 0.7 \Delta E_g$ for GaN/InGaN, and a bandgap bowing parameter of 1.4eV for InGaN. All the structures are pseudomorphic to GaN. The AlGaN interlayer leads to higher piezoelectric fields in the InGaN quantum well, but the higher barrier and sharper heterointerfaces lead to increased overlap, as shown in Figure 1. Knowing the wavefunction overlap is critical to understanding the recombination rates and performance, as shown below.

The second set is measured in various ways. The radiative efficiency ( $\eta_{\rm rad}$ ), differential carrier lifetime ( $\tau_{\rm DCL}$ ), and optical absorption are measured to determine the radiative rates. The  $\eta_{\rm rad}$  is the fraction of carriers that produce photons and is found by photoluminescence (PL) measured at both 8 K and room temperature with a 405 nm laser diode under continuous wave conditions and at power densities varying from  $\sim 5.5 \text{ W/cm}^2$  to  $\sim 18 \text{ kW/cm}^2$  [24], [39]. It is assumed that at 8 K and low input powers, the defects are frozen, and the  $\eta_{\rm rad}$  is 100% which has been found effective in InGaN/GaN MQWs [40]. Light spectra are measured using a high-resolution spectrometer. Optical absorption of the sample at 405 nm is measured by performing white light reflectance and transmission with an integrating sphere.

The differential carrier lifetimes are obtained by an alloptical measurement using methods similar to previous reports [24], [41]. The IL-MQW samples are excited with a 405 nm laser diode that is driven by combining (with a bias tee) a constant bias (constant carrier density) and small-signal sinusoidal bias frequencies between 0.05 and 500 MHz provided by a vector network analyzer (VNA).

The radiative  $(R_R)$  and non-radiative  $(R_{NR})$  recombination rates versus N are obtained by transforming the measured data and described previously [42], and in the following way. The generation rate, G, is defined by

$$G = P/(h\upsilon/q), \tag{1}$$

where P is the absorbed power density of the pump laser. The carrier density, N, is found integrating  $\tau_{DCL}$  with respect to G, expressed as

$$N = \int_0^G \tau_{DCL} dG. \tag{2}$$

Finally, the radiative and nonradiative rates are found using

$$\frac{dR_R}{dN} = \eta_{rad} \tau_{DCL}^{-1} + G \frac{d\eta_{rad}}{dN}, \qquad (3a)$$

$$\frac{dR_{NR}}{dN} = (1 - \eta_{rad}) \tau_{DCL}^{-1} - G \frac{d\eta_{rad}}{dN}. \qquad (3b)$$

$$\frac{dR_{NR}}{dN} = (1 - \eta_{rad}) \tau_{DCL}^{-1} - G \frac{d\eta_{rad}}{dN}.$$
 (3b)

Integrating Equations (3a) and (3b) versus N give the radiative and non-radiative rates versus the carrier density. From these rates, the SRH recombination coefficient A, radiative recombination coefficient, B and Auger defect recombination coefficient, C are determined [26] by

$$A = \frac{R_{NR}}{N}, \quad B = \frac{R_R}{N^2}, \quad C = \frac{(R_{NR} - AN)}{N^3}$$
 (4)

The A coefficient is valid and taken at low carrier densities  $(N < 10^{17} \text{ cm}^{-3})$  where SRH recombination dominates the non-radiative rate, and the equation for C is valid only at high carrier densities ( $N > 5 \times 10^{18} \text{ cm}^{-3}$ ) where Auger recombination dominates the non-radiative rate. The simple ABC model allows for estimation of the radiative efficiency,  $\eta_{\rm rad}$  using

$$\eta_{rad} = BN / (A + BN + CN^2) \tag{5}$$

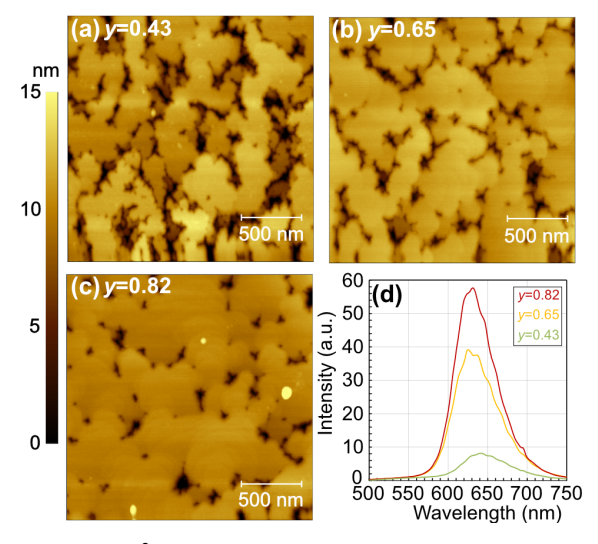


Fig. 2.  $2 \times 2 \mu m^2$  AFM images of IL-MQWs with an IL Al-content of (a) y = 0.43, (b) y = 0.65, and (c) y = 0.82. The surface morphology progressively improves with higher Al content in the IL. (d) PL spectra of the three samples. The y = 0.82 IL has the highest photoluminescence intensity.

which is the fraction of carriers injected into the quantum wells that produce light.

# III. RESULTS AND DISCUSSION

The effect of Al-content, y, of the  $Al_yGa_{1-y}N$  IL in the IL-MQW is studied first. Figs. 2(a)–(c) show the AFM images of the IL-MQW surfaces with y=0.43, 0.65, and 0.82. A clear improvement in surface morphology is observed with increasing y. The whole surface of the y=0.43 IL sample is covered with intersecting pits that originate from threading dislocations in the GaN template. For y=0.65, the pits still intersect, but the pit-free surface area is considerably larger. The y=0.82 sample surface has much smaller, well-formed pits and a smoother morphology [21]. Fig. 2(d) shows the PL spectra of the samples taken at room temperature with a 405 nm laser diode at a power density of  $\sim 600$  W/cm $^2$ . The PL intensity increases with increasing IL Al-content and is highest for y=0.82.

The improved morphology and light enhancement with high Al-content ILs is consistent with other studies [21]. These improvements are likely caused by better strain compensation provided by the higher Al composition and tensile strained IL [23], [24], as required with higher In-content and compressively strained QWs. Emitters in the green and yellow require lower Al-content interlayers [20, 22-24]. It is plausible that the higher In-content QW requires a higher Al-content IL to compensate for the strain effectively. IL-MQWs with y > 0.8 are used in the second set of LED structures based on this higher performance.

The results of measuring the second set of LEDs are shown in Fig. 3. First, Fig. 3(a) shows the  $\eta_{rad}$  versus pump power density. The IL-MQW grown on uid-GaN has a peak efficiency of 1.05% at  $\sim$ 4 kW/cm<sup>2</sup>. The IL-MQWs grown on the SL-ULs have different efficiencies. The peak  $\eta_{rad}$  are  $\sim$ 1.4%, 1.22%, and 0.94% for the IL-MQWs with SL-ULs grown at 850 °C (z=0.015) 850 °C (z=0.025), and 780 °C (z=0.065),

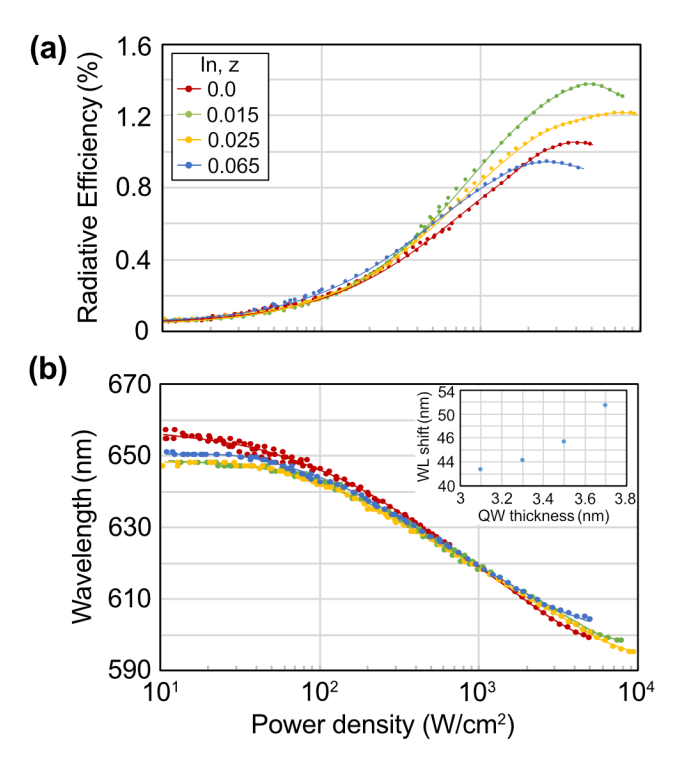


Fig. 3. Plots of (a)  $\eta_{rad}$  and (b) wavelength versus power density for IL-MQWs grown on GaN and  $In_zGa_{1-z}N/GaN$  superlattice underlayer with In-content of z=0.015, 0.025, and 0.065. The IL-MQW with z=0.015 has the highest peak efficiency. The inset shows the wavelength shift from 20 to 4000 W/cm² versus QW thickness. The wavelength blueshifts with increased power, and the blueshift decreases with thinner QWs.

respectively. This suggests that the SL-ULs play a role in the overall performance. The highest efficiency is for IL-MQW grown on the z = 0.015 SL-UL. The low radiative efficiencies of the MQWs are typical for red-emitting III-nitride LEDs [43], [44], [45], [46].

Figure 3(b) shows the wavelength shift versus power density. The samples emit at 658-648 nm (red) under low pump powers. Beyond  $\sim 100 \text{ W/cm}^2$ , enough carriers are created to observe a blueshift in the peak wavelength due to carrier screening and phase-space filling [47]. The wavelength shifts are different, and the blueshift from 20 to 4000 W/cm<sup>2</sup> versus the QW thickness is shown in the inset of Fig. 3(c). The thinner wells have a smaller blueshift due to quantum-confined Stark effect. The InGaN quantum wells at these high In content usually exhibit inhomogeneous compositions or worse In segregation. Lit images with a 405 nm laser of the MQWs show some spotty dark and green areas, indicating inhomogeneity. Another metric is the full width at half maximum (FWHM) of the spectra shown in Table I. The wider the FWHM, the more inhomogeneity. The highest FWHM is for the MQW without the underlayer. The FWHM is lower with an underlayer, ranging from 57 - 65 nm. The underlayer appears to improve inhomogeneity.

The measured radiative efficiency, absorption, and differential carrier lifetime are transformed into the radiative and non-radiative rates [24]. Fig. 4(a) shows the  $R_{NR}/N$  versus N. The total non-radiative recombination is caused by both SRH and Auger recombination. SRH recombination is dominant in

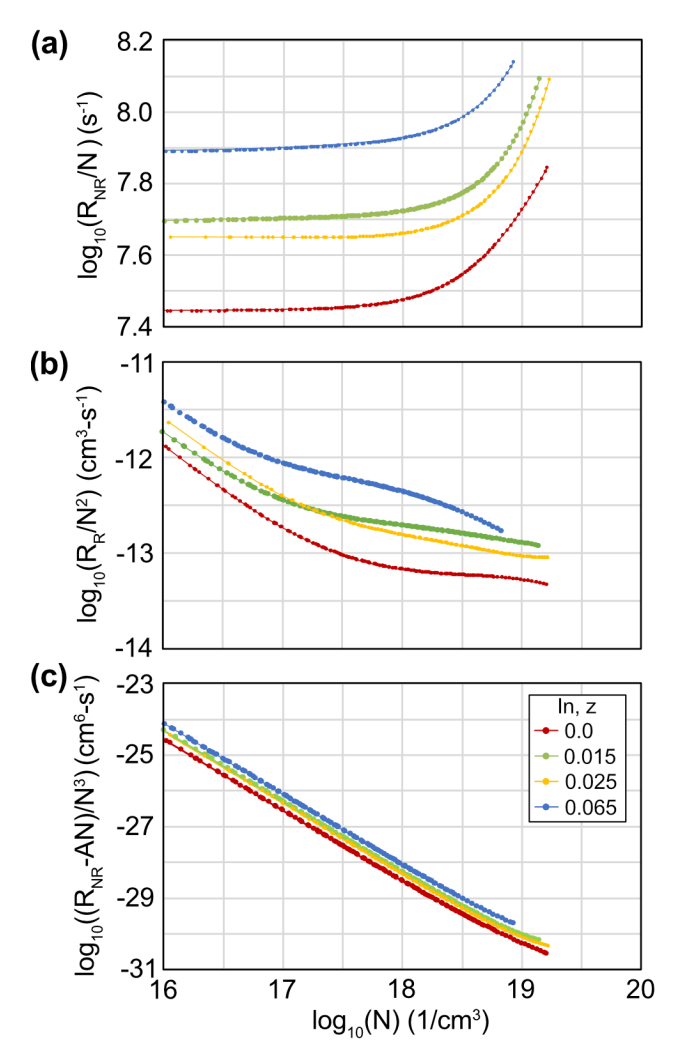


Fig. 4. Plots of the (a) nonradiative recombination rate ( $R_{NR}$ ) divided by steady-state carrier density (N) to give the A coefficients found at N=10<sup>16</sup>/cm<sup>2</sup>, (b) radiative recombination rate ( $R_R$ ) divided by N<sup>2</sup> to give the B coefficients found at N=3  $\times$  10<sup>18</sup> /cm<sup>3</sup>, and (c) ( $R_{NR}$ -AN)/N<sup>3</sup> versus N to give the C coefficients found at N=10<sup>19</sup> /cm<sup>3</sup>.

 $R_{NR}$  at low carrier densities and  $A=R_{NR}/N$  at low carrier densities, yielding the A coefficient. The IL-MQW grown on the uid-GaN UL has the lowest A coefficient of  $\sim 3.5 \times 10^7 \, \mathrm{s^{-1}}$  at  $\sim N = 5 \times 10^{16} \, \mathrm{cm^{-3}}$ . The IL-MQWs with SL-UL have higher A coefficients, at  $5.9 \times 10^7 \, \mathrm{s^{-1}}$ ,  $5.1 \times 10^7 \, \mathrm{s^{-1}}$ , and  $9.5 \times 10^7 \, \mathrm{s^{-1}}$  for z=0.015, 0.025, and 0.065, respectively. Possible causes (discussed further below) for these different values are the role of the SL-UL, changes in the number of defects, and wavefunction overlap in the QWs due to changes in polarization fields from layer and compositional differences.

Figure 4(b) shows the  $R_R/N^2$  versus N. The radiative recombination rate is the light-producing electron and hole recombination, and the  $R_R/N^2$  yields the value of the B coefficient (assuming  $R_R=BN^2$ ). The B coefficient varies with N due to multiple effects such as Coulomb interaction between electrons and holes, carrier screening, and phase-space filling [18], [37]. For comparisons to other reports, we take the B coefficient at  $N=3\times 10^{18}$  cm<sup>-3</sup>. The IL-MQW grown on uid-GaN UL has a  $B=5.9\times 10^{-14}$  cm<sup>3</sup>s<sup>-1</sup>, and the addition of the SL-ULs increases the B coefficient. The B

coefficient for InGaN/GaN SL-ULs with z=0.015, 0.025, and 0.065 are  $1.6 \times 10^{-13}$  cm<sup>3</sup>s<sup>-1</sup>,  $1.2 \times 10^{-13}$  cm<sup>3</sup>s<sup>-1</sup>, and  $2.8 \times 10^{-13}$  cm<sup>3</sup>s<sup>-1</sup>, respectively. One might expect the *B* coefficients for different samples in this study to have different values because of structural differences in the active region layers. It should be noted that these *B* coefficients are much lower than those measured at shorter wavelengths [24], [39], [42], [48], [49].

Figure 4(c) shows the  $(R_{NR}\text{-}AN)/N^3$  versus N, where the C coefficient is determined at high carrier densities.  $(R_{NR}\text{-}AN)$  is the Auger recombination rate portion of the total non-radiative recombination rate, which dominates at the high carrier densities  $(N \ge 5 \times 10^{18} \text{ cm}^{-3})$ . Therefore, the C coefficient is  $(R_{NR}\text{-}AN)/N^3$ , and its value is determined at  $N \sim 10^{19} \text{ cm}^{-3}$ . The C is  $5.9 \times 10^{-31} \text{ cm}^6 \text{s}^{-1}$  for the IL-MQW grown on GaN. The C coefficient for the IL-MQWs on InGaN/GaN SL-ULs with z=0.015, 0.025, and 0.065 are  $9.8 \times 10^{-31} \text{ cm}^6 \text{s}^{-1}$ ,  $7.8 \times 10^{-31} \text{ cm}^6 \text{s}^{-1}$ , and  $9.5 \times 10^{-31} \text{ cm}^6 \text{s}^{-1}$ , respectively. Overall, the IL-MQWs on SL-ULs have thinner QWs, higher A, B, and C coefficients, and higher radiative efficiency.

Comparing the A, B, and C coefficients to the overlap and each other provides insight into how structural differences between samples affect their values and  $\eta_{rad}$ . Fig. 5(a) shows a plot of the A coefficient versus the calculated overlap. As the overlaps increase from the decrease in QW thickness, the A coefficients increase too. The data fit a dependence of  $A \propto I^{1.3}$ . A dependence of A with respect to I was shown previously, and the exponent measured here is slightly higher (1.3 versus 1.2) [37]. The relationship between A and the overlap is attributed to the electron and hole wavefunction overlapping with a localized defect in the quantum well, and the defect has carrier cross-sectional terms that depend on I [41]. The A coefficient is also proportional to the number of QW defects which is important to note for the analysis below.

Fig. 5(b) shows a plot of the B coefficient versus the calculated overlap. The B coefficient increases with increased overlap caused by the thinner QW and fits a dependence of  $B \propto I^{2.1}$ . This dependence is close to the expected  $I^2$  for the B coefficient (radiative recombination rate) [50]. The close  $I^2$  relationship suggests that B varies as the layer thicknesses and composition of the QWs change the overlap. Other influences, such as a changing lattice constant caused by the SL-UL (as suggested by others [34]), are not used in the modeling and, therefore, are most likely not occurring (or a minor contributor) in these structures. Sources of error or differences with other reports include the simulation parameters used to calculate the overlap.

Both the A and B coefficients are functions of the overlap. To remove differences in the simulated overlap, one can compare A to B. This does not suggest a causal relationship between them, only that they both depend on the overlap. Fitting the data indicates that  $A \propto B^{0.64}$ . A dependence of  $A \propto B^{0.9}$  has been observed in InGaN-based QWs where the In-content or thickness changes [37], and is a consequence of changes in the polarization fields and the wavefunction overlap. The dependence here of A versus B is different and lower, implying that the SRH recombination is increasing at

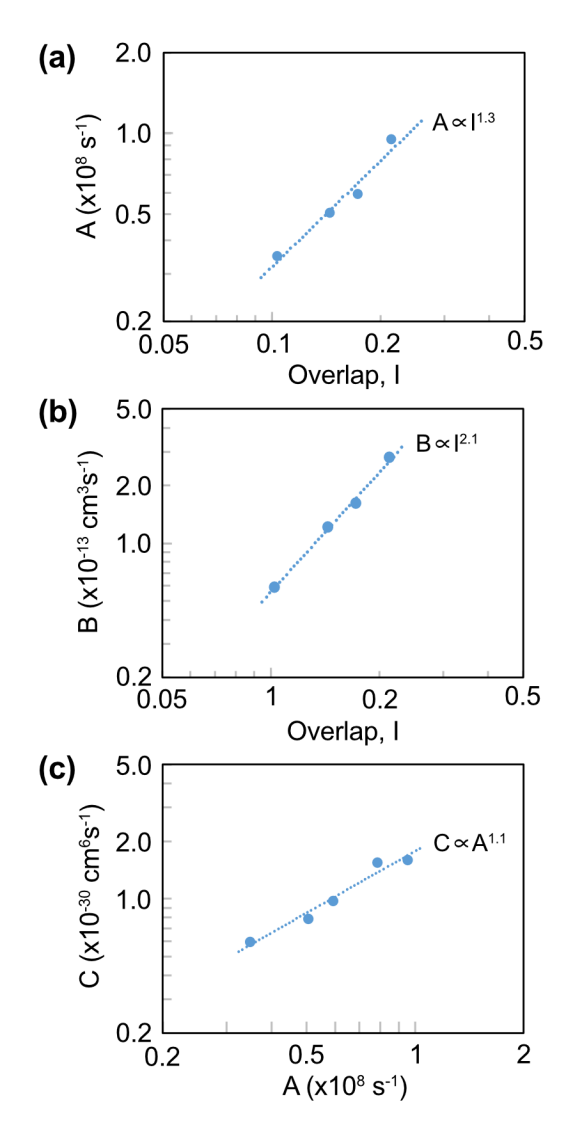


Fig. 5. Plots of (a) the A and (b) B coefficients versus the overlap. The overlap is simulated assuming the IL-MQW is pseudomorphic to GaN. The A and B show a dependence of A  $\propto$ I<sup>1.3</sup> and B $\propto$ I<sup>2.1</sup>. Plot of (c) A versus C coefficient of the IL-MQW samples. The relationship of A $\propto$ C<sup>1.1</sup> suggests that the trap-assisted process dominates the Auger recombination.

a lower rate. The IL-MQWs have not only thickness and alloy content changes but also the addition of the SL-UL with various In-content. One explanation is that the SL-UL also suppresses trap (defect) formation. This is consistent with other reports of lower defect formation when using an UL at shorter wavelengths [26], [27], [30]. Therefore, the SL-ULs used in this study also help to reduce defect formation in the red-emitting IL-MQWs. The defect formation could be reduced even more by optimizing the GaN barrier growth temperature [51]. Finally, the SL-UL could also improve inhomogeneity as suggested by the spectral FWHM.

Figure 5(c) is a plot of C versus A coefficients showing a power dependence of  $C \propto A^{1.1}$ . This is similar to the dependence observed in Ref. [36] when comparing A to C coefficients dominated by trap-assisted Auger recombination. Reports have suggested that the Auger recombination has two components: an intrinsic interband Auger recombination and an extrinsic defect-assisted Auger recombination [48]. The C

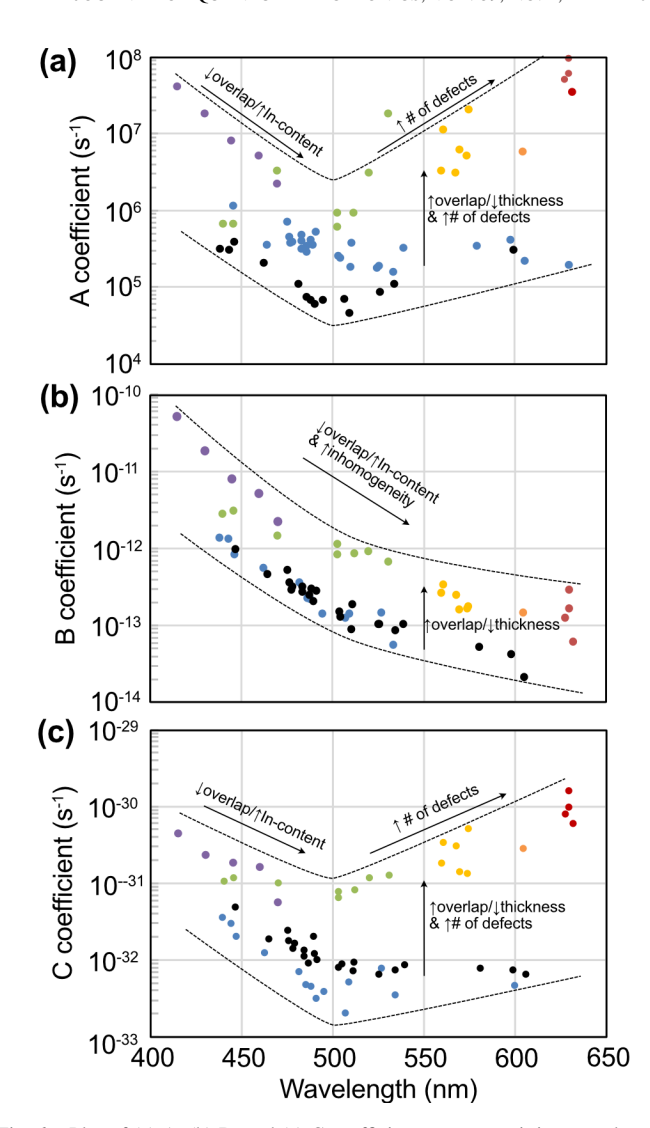


Fig. 6. Plot of (a) A, (b) B, and (c) C coefficients versus emitting wavelength for the red-emitting IL-MQWs (red) and from others (purple [42], blue [48], green [49], black [48], yellow [24], and orange [39]). The dashed lines are a guide for the eye to identify the spread (vertical direction) in the data caused by different MQW structures. The coefficients are affected by overlap changes due to In-content and thickness, the number of defects, and inhomogeneity.

coefficient plotted in Fig. 5(c) is a sum of all Auger processes, indicating that defects dominate Auger recombination in these structures. Reducing the number of defects at these high-Incontent QWs should improve both the *A* and *C* coefficients and the overall efficiency. The SL-UL helps to a small degree, so it may take more drastic structural changes, such as InGaN substrates [44], to see more significant improvements.

It is insightful to compare these red-emitting IL-MQWs at nearly the same In-content (x=0.27-0.29) to InGaN QWs emitting at shorter wavelengths with various In-content ( $x\sim0.1-0.29$ ). This gives a better understanding of the challenges InGaN emitters face as the In varies. Fig. 6 shows the A, B, and C coefficients versus emitting wavelength for the redemitting IL-MQWs (red circle) and data from other reports [24], [39], [42], [48], [49]. Due to the lack of information on layer structure or growth conditions in these references, an accurate direct comparison is difficult. However, dotted lines are provided, bounding the maximum and minimums,

to suggest trends in the data. The wide vertical variation observed in the data (at approximately the same In-content) is caused by overlap changes due to structural differences like QW thickness and the number of defects. Indeed, all the coefficients for the red-emitting IL-MQWs (red circles in Figure 6) increase as the QW thickness decreases and overlap increases (moving up in Figure 6 and up to the right in Figure 5). Variations moving horizontally at different wavelengths are primarily caused by changes in In-content, which affects the overlap and the number of defects. These determining factors, in both the vertical and horizontal directions, are further discussed for each coefficient.

Figure 6(a) shows the A coefficient decreasing as the wavelength increases from  $\sim$ 400 nm to  $\sim$ 500 nm by mainly raising the QW In-content, which leads to a reduction in the overlap. At wavelengths greater than 500 nm, the values have a wider vertical spread and increase. These two regions (< 500 nm and > 500 nm) are affected by the two dominant factors determining the A coefficient: the number of defects and the wavefunction overlap due to In-content. The steady decline in the A coefficient at < 500 nm results from decreasing overlap caused by higher-In-content QWs and higher polarization fields. This trend does not continue at >500 nm and results in higher A coefficients caused by a higher number of defects or some not yet identified mechanism [48].

The vertical variation in A coefficients is caused by overlap due to thickness changes and the number of defects. This variation is also more significant at longer wavelengths and can lead to higher A coefficients caused by an increasing number of defects. This trend suggesting some researchers are better at controlling defect formation than others due to structural or growth conditions.

Figure 6(b) shows the B coefficient drops with increasing wavelength as the In-content increases. The B coefficient is proportional to the transition energy, momentum matrix, and wavefunction overlap [50]. Increasing the In-content to produce blue to red wavelengths causes all three parameters to decrease. Still, the  $\sim$ 100 times decrease of the B coefficient is so large that it cannot be solely attributed to the decreasing wavefunction overlap from increased In-content and polarization fields. In addition, the wavefunction overlap is also affected by the inhomogeneity of the composition in the InGaN QW and carrier location [52], providing an additional knob at lowering overlap. As with the A coefficient, the spread in (vertical) values is caused by structural changes such as QW thickness. There is no upturn in B at longer wavelengths like A because it is not affected by defects.

Figure 6(c) shows the C coefficient decreasing as the wavelength increases from  $\sim$ 400 nm to  $\sim$ 500 nm. At wavelengths 500 nm, the values have a wider spread and increase. This trend is similar to the A coefficient and is not surprising because they are both affected by the overlap and the number of defects. At shorter wavelengths, Auger recombination is dominated by the intrinsic interband process, and the reduction in overlap leads to lower C coefficients. At > 500 nm, trapassisted Auger recombination dominates [48]. The increase in defects (traps), as indicated in the A coefficient (Fig. 6(a)), leads to higher C coefficients resulting in the same overall

trend. Therefore, controlling traps will lead to lower A and C coefficients and higher efficiencies in the red.

This work shows several pathways that should improve  $\eta_{\rm rad}$  (Equation 5) and overall efficiency. InGaN red emitters suffer from B coefficients that are at least 2 orders of magnitude lower than the blue. Active region and device structures that can increase wavefunction overlap will drastically improve B and  $\eta_{\rm rad}$ . While increasing overlap will also increase A and C, their increase will be lower than B because their dependence on overlap is at a lower rate (see Figure 5). Any structures that improve overlap should not increase the number of defects that would increase A and C beyond their overlap dependence. Future work should include exploring new IL materials like AlInN and AlInGaN for their greater strain engineering capabilities and higher overlap, and new barrier annealing conditions and growth steps for higher-quality ILs.

## IV. CONCLUSION

To conclude, red-emitting InGaN/AlGaN/GaN IL-MQWs and LEDs are grown to assess their recombination rates. High Al composition ( $y \ge 0.80$ ) ILs result in better morphology and higher PL efficiency, and the SL-UL aids in reducing defect formation. Still, the efficiencies compared to shorter wavelengths are relatively low due to low radiative recombination rates (B coefficients) and high nonradiative rates (A and C coefficients). Increases in efficiency can be achieved with higher wavefunction overlap, decreasing the number of defects, and improving compositional homogeneity. Future work should include exploring new IL materials like AlInN and AlInGaN for their greater strain engineering capabilities and higher overlap, and new barrier annealing conditions and growth steps for higher-quality ILs.

### REFERENCES

- [1] J. M. Phillips et al., "Research challenges to ultra-efficient inorganic solid-state lighting," *Laser Photon. Rev.*, vol. 1, no. 4, pp. 307–333, Dec. 2007, doi: 10.1002/lpor.200710019.
- [2] J. Y. Tsao et al., "Toward smart and ultra-efficient solid-state lighting," Adv. Opt. Mater., vol. 2, no. 9, pp. 809–836, 2014, doi: 10.1002/adom.201400131.
- [3] J. J. Wierer and N. Tansu, "III-nitride micro-LEDs for efficient emissive displays," *Laser Photon. Rev.*, vol. 13, no. 9, Sep. 2019, Art. no. 1900141, doi: 10.1002/lpor.201900141.
- [4] T. Wu et al., "Mini-LED and micro-LED: Promising candidates for the next generation display technology," *Appl. Sci.*, vol. 8, no. 9, p. 1557, Sep. 2018, doi: 10.3390/app8091557.
- [5] M. R. Krames et al., "Status and future of high-power light-emitting diodes for solid-state lighting," J. Display Technol., vol. 3, no. 2, pp. 160–175, Jun. 2007, doi: 10.1109/jdt.2007.895339.
- [6] T. Mukai, M. Yamada, and S. Nakamura, "Characteristics of InGaN-based UV/blue/green/amber/red light-emitting diodes," *Jpn. J. Appl. Phys.*, vol. 38, no. 7, pp. 3976–3981, 1999, doi: 10.1143/Jjap.38.3976.
- [7] D. D. Koleske, S. R. Lee, M. H. Crawford, K. C. Cross, M. E. Coltrin, and J. M. Kempisty, "Connection between GaN and InGaN growth mechanisms and surface morphology," *J. Cryst. Growth*, vol. 391, pp. 85–96, Apr. 2014, doi: 10.1016/j.jcrysgro.2014.01.010.
- [8] D. Cherns, S. J. Henley, and F. A. Ponce, "Edge and screw dislocations as nonradiative centers in InGaN/GaN quantum well luminescence," *Appl. Phys. Lett.*, vol. 78, no. 18, pp. 2691–2693, Apr. 2001, doi: 10.1063/1.1369610.
- [9] R. Singh, D. Doppalapudi, T. D. Moustakas, and L. T. Romano, "Phase separation in InGaN thick films and formation of InGaN/GaN double heterostructures in the entire alloy composition," *Appl. Phys. Lett.*, vol. 70, no. 9, pp. 1089–1091, Mar. 1997, doi: 10.1063/1.118493.

- [10] N. A. El-Masry, E. L. Piner, S. X. Liu, and S. M. Bedair, "Phase separation in InGaN grown by metalorganic chemical vapor deposition," *Appl. Phys. Lett.*, vol. 72, no. 1, pp. 40–42, Jan. 1998, doi: 10.1063/1.120639.
- [11] F. Nippert et al., "Determination of recombination coefficients in InGaN quantum-well light-emitting diodes by small-signal time-resolved photoluminescence," *Jpn. J. Appl. Phys.*, vol. 55, no. 5S, May 2016, Art. no. 05FJ01, doi: 10.7567/Jjap.55.05fj01.
- [12] S. Karpov, "Effect of carrier localization on recombination processes and efficiency of InGaN-based LEDs operating in the 'green gap," *Appl. Sci.*, vol. 8, no. 5, p. 818, May 2018, doi: 10.3390/app8050818.
- [13] M. Auf der Maur, A. Pecchia, G. Penazzi, W. Rodrigues, and A. Di Carlo, "Efficiency drop in green InGaN/GaN light emitting diodes: The role of random alloy fluctuations," *Phys. Rev. Lett.*, vol. 116, no. 2, Jan. 2016, Art. no. 027401, doi: 10.1103/Phys-RevLett.116.027401.
- [14] D. D. Koleske, A. E. Wickenden, R. L. Henry, and M. E. Twigg, "Influence of MOVPE growth conditions on carbon and silicon concentrations in GaN," *J. Cryst. Growth*, vol. 242, nos. 1–2, pp. 55–69, 2002, doi: 10.1016/S0022-0248(02)01348-9.
- [15] A. M. Armstrong, M. H. Crawford, and D. D. Koleske, "Contribution of deep-level defects to decreasing radiative efficiency of InGaN/GaN quantum wells with increasing emission wavelength," *Appl. Phys. Exp.*, vol. 7, no. 3, Mar. 2014, Art. no. 032101, doi: 10.7567/apex.7.032101.
- [16] V. Fiorentini, F. Bernardini, F. D. Sala, A. Di Carlo, and P. Lugli, "Effects of macroscopic polarization in III–V nitride multiple quantum wells," *Phys. Rev. B, Condens. Matter*, vol. 60, no. 12, pp. 8849–8858, Sep. 1999, doi: 10.1103/PhysRevB.60.8849.
- [17] H. Zhao, G. Liu, J. Zhang, J. D. Poplawsky, V. Dierolf, and N. Tansu, "Approaches for high internal quantum efficiency green InGaN lightemitting diodes with large overlap quantum wells," *Opt. Exp.*, vol. 19, no. S4, pp. A991–A1007, Jul. 2011, doi: 10.1364/OE.19.00A991.
- [18] U. T. Schwarz, H. Braun, K. Kojima, Y. Kawakami, S. Nagahama, and T. Mukai, "Interplay of built-in potential and piezoelectric field on carrier recombination in green light emitting InGaN quantum wells," *Appl. Phys. Lett.*, vol. 91, no. 12, Sep. 2007, Art. no. 123503, doi: 10.1063/1.2786602.
- [19] S. Saito, R. Hashimoto, J. Hwang, and S. Nunoue, "InGaN light-emitting diodes one-face sapphire substrates in green gap spectral range," *Appl. Phys. Exp.*, vol. 6, no. 11, Nov. 2013, Art. no. 111004, doi: 10.7567/Apex.6.111004.
- [20] R. Hashimoto, J. Hwang, S. Saito, and S. Nunoue, "High-efficiency yellow light-emitting diodes grown on sapphire (0001) substrates," *Phys. Status Solidi C*, vol. 11, nos. 3–4, pp. 628–631, Feb. 2014, doi: 10.1002/pssc.201300433.
- [21] J.-I. Hwang, R. Hashimoto, S. Saito, and S. Nunoue, "Development of InGaN-based red LED grown on (0001) polar surface," *Appl. Phys. Exp.*, vol. 7, no. 7, Jul. 2014, Art. no. 071003, doi: 10.7567/APEX.7.071003.
- [22] D. D. Koleske, A. J. Fischer, B. N. Bryant, P. G. Kotula, and J. J. Wierer, "On the increased efficiency in InGaN-based multiple quantum wells emitting at 530–590 nm with AlGaN interlayers," *J. Cryst. Growth*, vol. 415, pp. 57–64, Apr. 2015, doi: 10.1016/j.jcrysgro.2014.12.034.
- [23] S. A. Al Muyeed et al., "Strain compensation in InGaN-based multiple quantum wells using AlGaN interlayers," AIP Adv., vol. 7, no. 10, Oct. 2017, Art. no. 105312, doi: 10.1063/1.5000519.
- [24] S. A. Al Muyeed et al., "Recombination rates in green-yellow InGaN-based multiple quantum wells with AlGaN interlayers," *J. Appl. Phys.*, vol. 126, no. 21, Dec. 2019, Art. no. 213106, doi: 10.1063/1.5126965.
- [25] S. R. Lee, D. D. Koleske, M. H. Crawford, and J. J. Wierer, "Effect of interface grading and lateral thickness variation on X-ray diffraction by InGaN/GaN multiple quantum wells," *J. Cryst. Growth*, vol. 355, no. 1, pp. 63–72, Sep. 2012, doi: 10.1016/j.jcrysgro.2012.06.048.
- [26] A. M. Armstrong, B. N. Bryant, M. H. Crawford, D. D. Koleske, S. R. Lee, and J. J. Wierer, "Defect-reduction mechanism for improving radiative efficiency in InGaN/GaN light-emitting diodes using InGaN underlayers," *J. Appl. Phys.*, vol. 117, no. 13, 2015, Art. no. 262101, doi: 10.1063/1.4916727.
- [27] C. Haller, J.-F. Carlin, G. Jacopin, D. Martin, R. Butté, and N. Grandjean, "Burying non-radiative defects in InGaN underlayer to increase InGaN/GaN quantum well efficiency," *Appl. Phys. Lett.*, vol. 111, no. 26, Dec. 2017, Art. no. 262101, doi: 10.1063/ 1.5007616.
- [28] C. Haller, J.-F. Carlin, M. Mosca, M. D. Rossell, R. Erni, and N. Grandjean, "InAlN underlayer for near ultraviolet InGaN based light emitting diodes," *Appl. Phys. Exp.*, vol. 12, no. 3, Feb. 2019, Art. no. 034002, doi: 10.7567/1882-0786/ab0147.

- [29] Y. Chen, C. Haller, W. Liu, S. Y. Karpov, J.-F. Carlin, and N. Grandjean, "GaN buffer growth temperature and efficiency of InGaN/GaN quantum wells: The critical role of nitrogen vacancies at the GaN surface," *Appl. Phys. Lett.*, vol. 118, no. 11, Mar. 2021, Art. no. 111102, doi: 10.1063/5.0040326.
- [30] C. Haller et al., "GaN surface as the source of non-radiative defects in InGaN/GaN quantum wells," Appl. Phys. Lett., vol. 113, no. 11, Sep. 2018, Art. no. 111106, doi: 10.1063/1.5048010.
- [31] A. Hangleiter et al., "Suppression of nonradiative recombination by V-shaped pits in GaInN/GaN quantum wells produces a large increase in the light emission efficiency," *Phys. Rev. Lett.*, vol. 95, no. 12, Sep. 2005, Art. no. 127402, doi: 10.1103/PhysRevLett.95.127402.
- [32] D.-H. Lee, D. Kang, T.-Y. Seong, M. Kneissl, and H. Amano, "Effect of unevenly-distributed V pits on the optical and electrical characteristics of green micro-light emitting diode," *J. Phys. D, Appl. Phys.*, vol. 53, no. 4, Jan. 2020, Art. no. 045106, doi: 10.1088/1361-6463/ab52d0.
- [33] F. Jiang et al., "Efficient InGaN-based yellow-light-emitting diodes," Photon. Res., vol. 7, no. 2, pp. 144–148, Feb. 2019, doi: 10.1364/PRJ.7.000144.
- [34] S. Kusanagi, Y. Kanitani, Y. Kudo, K. Tasai, A. A. Yamaguchi, and S. Tomiya, "InGaN quantum wells with improved photoluminescence properties through strain-controlled modification of the InGaN underlayer," *Jpn. J. Appl. Phys.*, vol. 58, Jun. 2019, Art. no. SCCB28, doi: 10.7567/1347-4065/ab0f11.
- [35] T. Li et al., "The effect of InGaN underlayers on the electronic and optical properties of InGaN/GaN quantum wells," Appl. Phys. Lett., vol. 102, no. 4, Jan. 2013, Art. no. 041115, doi: 10.1063/ 1.4789758
- [36] M. S. Kumar, J. Y. Park, Y. S. Lee, S. J. Chung, C.-H. Hong, and E.-K. Suh, "Effect of barrier growth temperature on morphological evolution of green InGaN/GaN multi-quantum well heterostructures," *J. Phys. D, Appl. Phys.*, vol. 40, no. 17, pp. 5050–5054, Sep. 2007, doi: 10.1088/0022-3727/40/17/007.
- [37] A. David, N. G. Young, C. Lund, and M. D. Craven, "Review— The physics of recombinations in III-nitride emitters," ECS J. Solid State Sci. Technol., vol. 9, no. 1, Jan. 2020, Art. no. 016021, doi: 10.1149/2.0372001jss.
- [38] S. Birner et al., "nextnano: General purpose 3-D simulations," *IEEE Trans. Electron Devices*, vol. 54, no. 9, pp. 2137–2142, Sep. 2007, doi: 10.1109/TED.2007.902871.
- [39] S. A. A. Muyeed et al., "Recombination rates of  $In_xGa_{1-x}N/Al_yGa_{1-y}N/GaN$  multiple quantum wells emitting from 640 to 565 nm," *IEEE J. Quantum Electron.*, vol. 57, no. 6, pp. 1–7, Dec. 2021, doi: 10.1109/jqe.2021.3111402.
- [40] S. Sidikejiang et al., "Low-temperature internal quantum efficiency of GaInN/GaN quantum wells under steady-state conditions," *Semi*cond. Sci. Technol., vol. 37, no. 3, Mar. 2022, Art. no. 035017, doi: 10.1088/1361-6641/ac4b89.
- [41] A. David, C. A. Hurni, N. G. Young, and M. D. Craven, "Field-assisted Shockley-Read-Hall recombinations in III-nitride quantum wells," *Appl. Phys. Lett.*, vol. 111, no. 23, Dec. 2017, Art. no. 233501, doi: 10.1063/1.5003112.
- [42] A. David and M. J. Grundmann, "Droop in InGaN light-emitting diodes: A differential carrier lifetime analysis," *Appl. Phys. Lett.*, vol. 96, no. 10, Mar. 2010, Art. no. 103504, doi: 10.1063/1.3330870.
- [43] J. Hwang, R. Hashimoto, and S. Saito, "Green, yellow, and red LEDs," in III-Nitride Based Light Emitting Diodes and Applications, T.-Y. Seong, J. Han, H. Amano, and H. Morkoç, Eds. Singapore: Springer, 2017, pp. 239–266.
- [44] A. Dussaigne et al., "Full InGaN red (625 nm) micro-LED (10  $\mu$ m) demonstration on a relaxed pseudo-substrate," *Appl. Phys. Exp.*, vol. 14, no. 9, Sep. 2021, Art. no. 092011, doi: 10.35848/1882-0786/ac1b3e.
- [45] Z. Zhuang, D. Iida, and K. Ohkawa, "Investigation of InGaN-based red/green micro-light-emitting diodes," Opt. Lett., vol. 46, no. 8, pp. 1912–1915, 2021, doi: 10.1364/ol.422579.
- [46] D. Iida, Z. Zhuang, P. Kirilenko, M. Velazquez-Rizo, M. A. Najmi, and K. Ohkawa, "633-nm InGaN-based red LEDs grown on thick underlying GaN layers with reduced in-plane residual stress," *Appl. Phys. Lett.*, vol. 116, no. 16, Apr. 2020, Art. no. 162101, doi: 10.1063/1.5142538.
- [47] J. Zhang and N. Tansu, "Improvement in spontaneous emission rates for InGaN quantum wells on ternary InGaN substrate for light-emitting diodes," *J. Appl. Phys.*, vol. 110, no. 11, Dec. 2011, Art. no. 113110, doi: 10.1063/1.3668117.

- [48] A. David, N. G. Young, C. A. Hurni, and M. D. Craven, "Quantum efficiency of III-nitride emitters: Evidence for defect-assisted nonradiative recombination and its effect on the green gap," *Phys. Rev. Appl.*, vol. 11, no. 3, Mar. 2019, Art. no. 031001, doi: 10.1103/PhysRevApplied.11.031001.
- [49] D. Schiavon, M. Binder, M. Peter, B. Galler, P. Drechsel, and F. Scholz, "Wavelength-dependent determination of the recombination rate coefficients in single-quantum-well GaInN/GaN light emitting diodes," *Phys. Status Solidi B*, vol. 250, no. 2, pp. 283–290, 2013, doi: 10.1002/pssb.201248286.
- [50] S. L. Chuang, Physics of Photonic Devices (Wiley Series in Pure and Applied Optics), 2nd ed. Hoboken, NJ, USA: Wiley, 2009, p. 821.
- [51] C. Haller et al., "GaN surface as the source of non-radiative defects in InGaN/GaN quantum wells," Appl. Phys. Lett., vol. 113, no. 11, Sep. 2018, Art. no. 111106, doi: 10.1063/1.5048010.
- [52] C. M. Jones, C.-H. Teng, Q. Yan, P.-C. Ku, and E. Kioupakis, "Impact of carrier localization on recombination in InGaN quantum wells and the efficiency of nitride light-emitting diodes: Insights from theory and numerical simulations," *Appl. Phys. Lett.*, vol. 111, no. 11, Sep. 2017, Art. no. 113501, doi: 10.1063/1.5002104.

**Haotian Xue** received the B.S. degree in applied physics from the University of Science and Technology of China and the M.S. degree in electrical engineering from Lehigh University in 2020. He is currently pursuing the Ph.D. degree with North Carolina State University, researching the growth of III-Nitride semiconductors for power devices and light emitters.

**Syed Ahmed Al Muyeed** received the B.S. and M.S. degrees from the Department of Electrical and Electronic Engineering, University of Dhaka, Bangladesh, in 2014 and 2016, respectively, and the Ph.D. degree in electrical engineering from Lehigh University, in May 2021. He is currently a member of the Technical Staff at Google, Fremont, CA, USA. His research interests include the physics, growth, and characterization of III-Nitride semiconductor light emitters, especially in the visible range.

Elia Palmese received the B.S. degree in electrical engineering from Villanova University in 2019. He is currently pursuing the Ph.D. degree with North Carolina State University. He is currently conducting research in III-Nitride power electronics and semiconductor devices. Specifically, he is working on the oxidation of AlInN and TCAD modeling of GaN power devices.

**Daniel Rogers** received the B.S. degree in physics from Seton Hall in 2020. He is currently pursuing the Ph.D. degree with North Carolina State University. He is currently researching III-Nitride light emitters.

**Renbo Song** received the B.S. and M.S. degrees in optics and condensed matter physics from Shandong University, China, in 1998 and 2001, respectively, and the Ph.D. degree in electrical engineering from Lehigh University, Bethlehem, PA, USA, in 2009. He worked as an MOCVD Scientist for Valence Process Equipment from 2011 to 2015, and since then, he has been the Scientific Manager of the Lehigh University. His areas of interests include MOCVD and new epitaxy technologies for wide bandgap semiconductors.

Nelson Tansu (Fellow, IEEE) received the B.S. and Ph.D. degrees from the University of Wisconsin-Madison in 1998 and 2003, respectively. He is currently the Head of the School and a Professor of quantum electronics with the School of Electrical and Mechanical Engineering, The University of Adelaide (Adelaide, South Australia, and Australia). From July 2003 to January 2021, he was the Daniel E. '39 and the Patricia M. Smith Endowed Chair Professor with the Department of Electrical and Computer Engineering (ECE), and the Director for the Center for Photonics and Nanoelectronics (CPN), Lehigh University. He had made seminal advances to the invention and innovation, fundamental sciences, and device technologies of III-V and III-Nitride semiconductors. He has more than 18 U.S. patents, and his work is integrated in today's state-of-the-art solid-state lighting technology. He has authored more than 165 refereed journals and 325 conference publications. He was served as a member for the Editorial Boards for eight other leading journals in applied physics and nanotechnology. He is a fellow of the U.S. National Academy of Inventors (NAI Fellow; elected in 2016) and a Clarivate Analytics Highly Cited Researcher (in 2018). He is the Editor-in-Chief of the Open Access Journal Photonics.

Jonathan J. Wierer, Jr. (Senior Member, IEEE) received the B.S., M.S., and Ph.D. degrees in electrical engineering from the University of Illinois, Urbana–Champaign, IL, USA, in 1994, 1995, and 1999, respectively. He is currently a Professor with the Department of Electrical and Computer Engineering, North Carolina State University, Raleigh, NC, USA. Previously, he was with Philips-Lumileds, San Jose, CA, USA; Sandia National Laboratories, Albuquerque, NM, USA; and Lehigh University, Bethlehem, PA, USA. His research highlights include developing the first high-power (1 Watt) flip-chip Ill-nitride LED and proposing laser diodes as an ultra-efficient light source for solid-state lighting. He has authored or coauthored over 180 publications and conference publications and holds 42 patents, predominately related to III-nitride devices. He is a Senior Editor for the IEEE Photonics Technology Letters.